Scripta Materialia 182 (2020) 81–85

Contents lists available at ScienceDirect

Scripta Materialia

journal homepage: www.elsevier.com/locate/scriptamat

Microstructural characterization of dendritic evolution using two-point statistics

Kate L.M. Elder[a], Tiberiu Stan[a], Yue Sun[a], Xianghui Xiao[b,c], Peter W. Voorhees[a,*]

[a] Department of Materials Science and Engineering, Northwestern University, Evanston, IL 60208, USA
[b] Advanced Photon Source, Argonne National Laboratory, Lemont, IL 60439, USA
[c] National Synchrotron Light Source II (NSLS-II), Brookhaven National Laboratory, Upton, NY 11973, USA

ARTICLE INFO

Article history:
Received 8 February 2020
Revised 19 February 2020
Accepted 19 February 2020

Keywords:
Dendritic growth
Two-point statistics
Three-dimensional tomography
Solidification microstructure
Aluminum alloys

ABSTRACT

Characterizing large four-dimensional materials datasets is difficult due to the presence of complex microstructures and time-varying length scales. We showcase the use of two-point statistics as an efficient and un-biased way of extracting materials parameters from an Al-Cu alloy during solidification. The evolution of dendrite primary arm thickness, average secondary arm spacing, and average tip-to-tip spacing were tracked using two-point Pearson auto-correlations of scaled mean curvatures. Insights into competitive side-branching are also reported. We show both visually and quantitatively that most length scales change rapidly during early stages of dendritic growth, but slow as diffusion fields of dendrites overlap.

The dendritic microstructures that form during solidification of metallic alloys are central to setting electronic, magnetic and mechanical properties [1,2]. In particular, the secondary dendrite arm spacing (SDAS) has substantial influence on alloy hardness and tensile strength [3,4]. In addition, the secondary arm tip-to-tip spacing (TS) can be used to quantify the degree of competitive side-branch behavior in dendritic evolution [5,6]. Many in-situ solidification experiments and phase field simulations result in large four-dimensional datasets (three spatial dimensions and time) that are difficult to analyze. The dendritic morphologies are often characterized using interfacial shape distributions [7,8] and interface normal distributions [9,10]. However, these techniques provide no information regarding length scales in the structure. Important properties such as the SDAS are often manually identified from two-dimensional slices of the microstructure [11]. This procedure is subject to human error, user-to-user variability, and dependence on section orientation. Two-point statistics techniques have emerged as an efficient and un-biased way of characterizing four-dimensional datasets. The methods have been used to identify microstructural spacings during coarsening of dendrites [12,13] and bicontinuous structures [14,15]. Applying this method to in-situ solidification data, we use two-point statistics of interfacial curvatures to characterize primary and secondary dendrite arm evolution during dendritic growth.

Four-dimensional X-ray computed tomography (XCT) was used to study dendritic growth in an Al-12.6 wt.% Cu alloy. Experiments were performed at Argonne National Laboratory, Advanced Photon Source, beamline 2-BM [1]. A 5 mm tall, 1.2 mm diameter cylindrical sample was inserted into an X-ray transparent boron-nitride holder and placed within the incident X-ray beam. The assembly was then held at a temperature above the liquidus (~ 630°C) to ensure that the alloy was fully melted, and rotated at a slew speed of 72 degrees/second. The sample was then cooled at 1°C/minute and the dendritic growth was recorded from ~ 625°C to ~ 540°C. This process results in a freely growing dendrite that has not been influenced to grow in a particular orientation, unlike directional solidification experiments [16]. The start of recording is considered time zero and all referenced times are post recording. Time-Interlaced Model-Based Iterative Reconstruction (TIMBIR) [17] was used to reconstruct the projections into a series of three-dimensional volumes with 1.95 μm^3 voxel size and 10 second temporal resolution. Otsu's method was used to segment the Al dendrites from the Al-Cu liquid phases [18] and MATLAB was used for meshing and statistical calculations. While the triangular mesh patches vary in size along the complex solid-liquid interfaces, the average patch area is 5.62 μm^2. This work analyzes dendritic growth times between 50 and 290 s.

* Corresponding author.
E-mail address: p-voorhees@northwestern.edu (P.W. Voorhees).

https://doi.org/10.1016/j.scriptamat.2020.02.034
1359-6462/

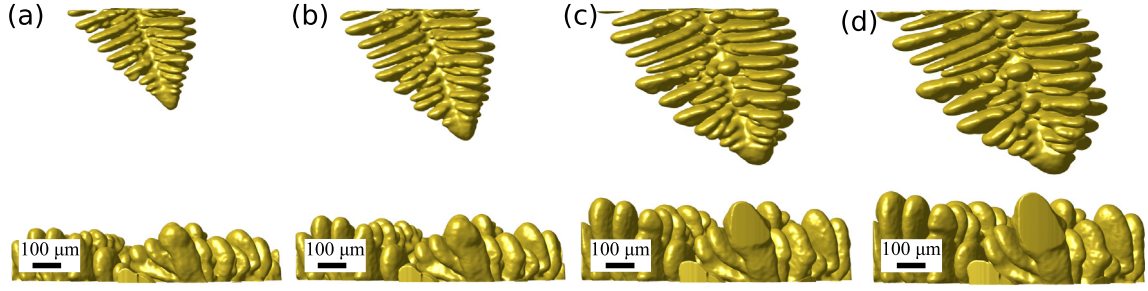

Fig. 1. Downward growing Al-rich dendrite and upward-growing seaweed structures at (a) 50 s, (b) 90 s, (c) 170 s, and (d) 270 s. A video of the time evolution is available in the supplemental information.

A video of the observed growth can be found in the supplemental information. Fig. 1a–d shows the microstructures at 50 s, 90 s, 170 s, and 270 s. A single-crystal Al-rich dendrite grows from the top of the sample toward the multiple seaweed-like dendrites at the bottom. The velocity (v) of the dendrite tip decays from ~ 3 μm/s and reaches an approximately constant value of ~ 0.4 μm/s at 160 s. At later times, the top dendrite velocity is slowed largely due to increased interactions with the bottom structures. The concentration profile ahead of a solidifying front has an approximate characteristic length $L = D/v$ [19], where D is the solute diffusivity in the liquid. Values in the literature for D range from ~ 830 $\mu m^2/s$ to ~ 6000 $\mu m^2/s$ [20–24]. It is assumed that two solidifying fronts interact if their separation is less than $2L$. As early as 50 s, and assuming the smallest D (830 $\mu m^2/s$ [21]), $2L \approx 520$ μm and the distance between the dendrite and seaweed is $\approx$ 430 μm. Thus, the dendrite begins in free growth but the two diffusion fields likely interact at all observed times (50 to 290 s). As seen in Fig. 1, manually measuring length scales of interest, such as SDAS and TS, at each time step would be laborious for these complex microstructures.

Fig. 2a shows an alternate view of the dendrite in Fig. 1c, sliced by planes along the dendrite axis. A level-set method [25] was used to calculate the mean curvature (H) at each mesh vertex along the dendrite surface where $H = (\kappa_1 + \kappa_2)/2$; κ_1 and κ_2 are the principal curvatures. The mesh is colored according to the scaled mean curvature (H/S_V), where S_V is the total interfacial area per dendrite volume. Areas of low and negative mean curvature are found along the root of the primary arm and in spaces between secondary arms. High mean curvature regions mostly correspond to the primary, secondary, and tertiary arm tips.

The Al dendrite in Fig. 2a is sliced by planes along the orthogonal $\boldsymbol{n_1}$, $\boldsymbol{n_2}$, and $\boldsymbol{n_3}$ axes. The vector $\boldsymbol{n_3}$ is the dendrite growth direction. Fig. 2b shows the cross section along the $\boldsymbol{n_1} - \boldsymbol{n_2}$ plane and Fig. 2c shows the cross section along the $\boldsymbol{n_2} - \boldsymbol{n_3}$ plane. The slices are positioned such that the $\boldsymbol{n_1} - \boldsymbol{n_3}$ and $\boldsymbol{n_2} - \boldsymbol{n_3}$ planes intersect along the primary arm core, and the $\boldsymbol{n_1} - \boldsymbol{n_2}$ plane is 281 μm from the dendrite tip. The slices are colored according to the signed distance function (SDF), which indicates the distance to the nearest solid-liquid interface at each point in space [26]. Positive SDF values indicate solid Al dendrite, negative values represent the Al-Cu liquid, and the interface is defined at 0. The SDF along the $\boldsymbol{n_1} - \boldsymbol{n_2}$ plane in Fig. 2b shows the primary arm with four secondary arms. Fig. 2c shows the SDF in the $\boldsymbol{n_2} - \boldsymbol{n_3}$ plane, which cuts along the center of the primary arm.

Two-point statistics were used to extract information about the spatial distribution of microstructural features. Of particular interest is the Pearson correlation function [12], which gives the probability that a local attribute is the same when separated by a spatial vector. This function ranges from -1 to 1, where -1 is perfect anti-correlation, 0 is no correlation, and 1 is perfect correlation. Recent work from Sun et. al. [12] extended two-point statistics methods to capture correlations of interfacial quantities (mean curvatures, Gaussian curvatures, velocities). We used a discretized two-point Pearson correlation [12] to calculate auto-correlations of the scaled interface mean curvature. The interfacial patches were first discretized into five equally sized bins each containing 20% of the curvature values by area. Patches from the bin with the lowest curvature values were isolated for primary arm analysis (example in Fig. 3), and patches from the bin with the highest mean curvature were isolated for secondary arm analysis (example in Fig. 4). The H auto-correlation was calculated in three-dimensions at each time step using a cutoff distance of 390 μm in each direction. Thus the H auto-correlation is calculated for patches of interface that are separated by distances less than or equal to 390 μm.

Fig. 3a shows a 20 μm thick portion of the same dendrite as in Fig. 2a, centered around the $\boldsymbol{n_1} - \boldsymbol{n_2}$ plane in Fig. 2b. Low curvature regions (from the bin with the lowest 20% of curvature values) are highlighted in pink, and all other curvatures are colored tan. The H auto-correlation between the pink and tan regions is shown in Fig. 3b, along the $\boldsymbol{n_1} - \boldsymbol{n_2}$ plane. Details of how H auto-correlation maps are generated and interpreted are found in references [12,15]. In summary, the map center is the zero point and the x- and y-axis range from -244 μm to 244 μm for Fig. 3b. Local maxima in the map correspond to characteristic microstructural length scales and directions. Dark red regions indicate high correlations (pink-to-pink and tan-to-tan), white regions indicate no correlation, and blue regions indicate large anti-correlations (pink-to-tan). The three colored arrows in Fig. 3a and 3b represents the size of the primary arm in the $\boldsymbol{n_2}$ direction (dark green - 62 ± 4 μm), the size of the primary arm in the $\boldsymbol{n_1}$ direction (teal - 76 ± 4 μm), and the width of the primary arm in the $-\boldsymbol{n_1}$, $+\boldsymbol{n_2}$ direction (black - 111 ± 2 μm). The error is defined as the radius of the local region consisting of values that are less than 20% different from the local maxima in the H auto-correlation.

The H auto-correlation was also used to measure the primary arm width in the $-\boldsymbol{n_1}$, $+\boldsymbol{n_2}$ direction throughout the dendrite evolution. The $\boldsymbol{n_1} - \boldsymbol{n_2}$ plane was held at a fixed position, 490 μm below the top of the viewing window, and cross sections were captured at each time step. Fig. 3c shows the dendrite interface along the referenced plane at 50 s (dark blue outline corresponding to Fig. 1a), 90 s (orange outline corresponding to Fig. 1b), and 270 s (grey outline corresponding to Fig. 1d). The black arrows indicate the direction along which the primary arm width was measured. Fig. 3d shows the arm width as a function of time, obtained computationally by extracting the H auto-correlation local maximum in the $-\boldsymbol{n_1}$, $+\boldsymbol{n_2}$ direction. The dark blue, orange, and grey boxes correspond to the same times as the interface cross sections in Fig. 3c. The H auto-correlation confirms the small primary arm width at 50 s (53 ± 3 μm), large increase at 90 s (93 ± 2 μm), and smaller increase at 270 s (120 ± 3 μm). As the viewing plane is held at a constant height in the lab frame, these calculations first capture the size of the dendrite tip. As the dendrite keeps growing, Fig. 1, the same plane in the lab frame now captures information about primary dendrite arm width, accounting for the large change in

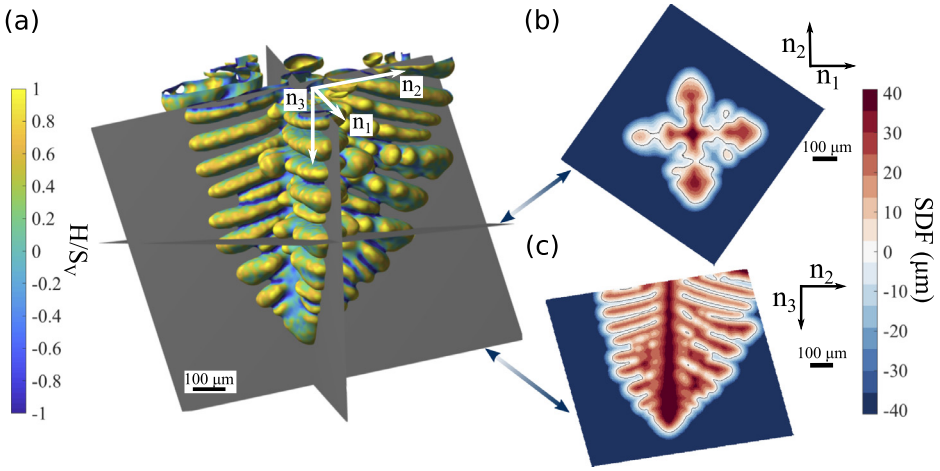

Fig. 2. Illustration of the dendrite axis for the Al dendrite at 170 s showing (a) the isosurface colored by the scaled mean curvature, sliced by the $\boldsymbol{n_1} - \boldsymbol{n_2}$, $\boldsymbol{n_1} - \boldsymbol{n_3}$, and $\boldsymbol{n_2} - \boldsymbol{n_3}$ planes; (b) the SDF in the $\boldsymbol{n_1} - \boldsymbol{n_2}$ plane; and (c) the SDF in the $\boldsymbol{n_2} - \boldsymbol{n_3}$ plane. Slices are positioned such that the $\boldsymbol{n_1} - \boldsymbol{n_3}$ and $\boldsymbol{n_2} - \boldsymbol{n_3}$ planes intersect at the core of the primary arm and the center of the $\boldsymbol{n_1} - \boldsymbol{n_2}$ plane is 281 μm from the dendrite tip. (For interpretation of the references to color in this figure, the reader is referred to the web version of this article.)

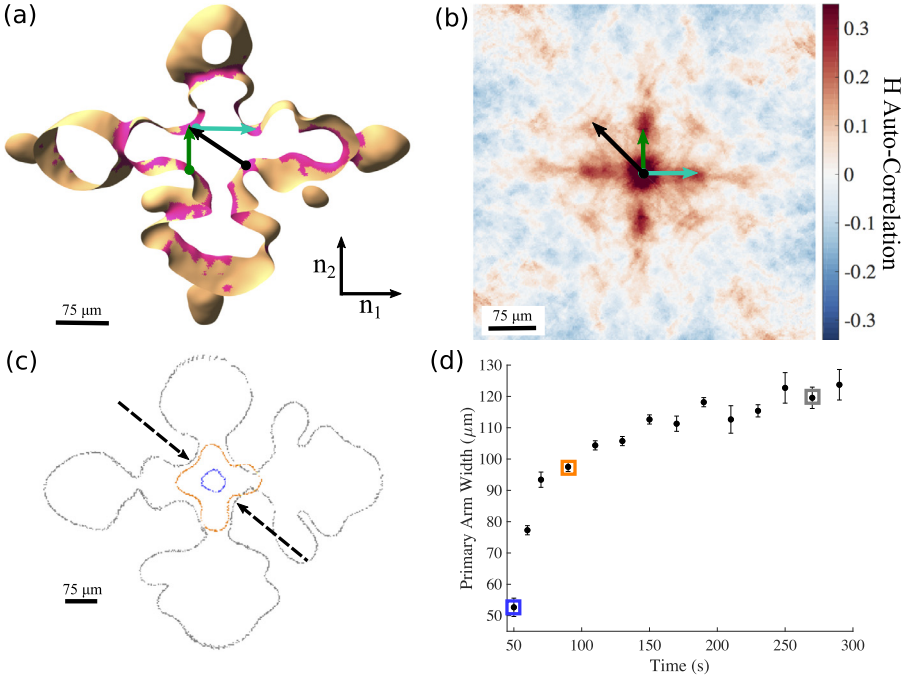

Fig. 3. (a) 20 μm thick portion of the Al dendrite centered around the $\boldsymbol{n_1} - \boldsymbol{n_2}$ plane (Fig. 2b) at 170 s. Pink areas correspond to the bottom 20% mean curvature values and all other curvatures are colored tan; (b) H auto-correlation of the pink and tan regions in (a). The arrows in (a,b) have length of 62 μm (dark green), 76 μm (teal), and 111 μm (black). (c) Dendrite outline in the $\boldsymbol{n_1} - \boldsymbol{n_2}$ plane located 490 μm from the top of the viewing window at 50 s (dark blue), 90 s (orange), and 270 s (grey). The black dashed arrows indicate the direction the primary arm width is calculated in; and (d) primary arm width as a function of time. The dark blue, orange, and grey boxes correspond to the outlines in (c). (For interpretation of the references to color in this figure, the reader is referred to the web version of this article.)

primary arm width at early times. As the growth velocity slows, the primary arm width continues to increase slightly in time.

While characterizing the primary dendrite arm width demonstrated the robustness of using Pearson correlations on four-dimensional microstructures, the two-point statistics method was also used to measure global microstructural properties which cannot be easily measured on the dendrite: the average TS and average SDAS. Fig. 4a shows the dendrite at 170 s, same as in Figs. 1c and 2a. The dark green portions of the isosurface represent the curvature patches from the bin with the highest 20% of curvature values as they are primarily found at secondary arm tips and emerging tertiary arms. The SDAS is measured parallel to the primary arm growth direction ($\boldsymbol{n_3}$), and indicated in Fig. 4a using a teal vertical arrow. The black arrow in Fig. 4a indicates one TS. The arms at the top of the structure form first and are longer than those at the bottom, thus the TS vector is at an angle with respect to the growth direction.

In contrast to the primary arm thickness measurement where the analysis plane was fixed in the lab frame, the SDAS and TS evolution was measured near the continuously moving dendrite tip. The curvatures within a 390 μm box above the dendrite tip were analyzed at each time step. The H auto-correlation in Fig. 4b was obtained by characterizing the structure at 170 s (Fig. 4a) along the $\boldsymbol{n_2} - \boldsymbol{n_3}$ plane. The distance from the center of the H auto-correlation to the first local maximum along the vertical direction (teal arrow) corresponds to the average SDAS (31 ± 2 μm). The

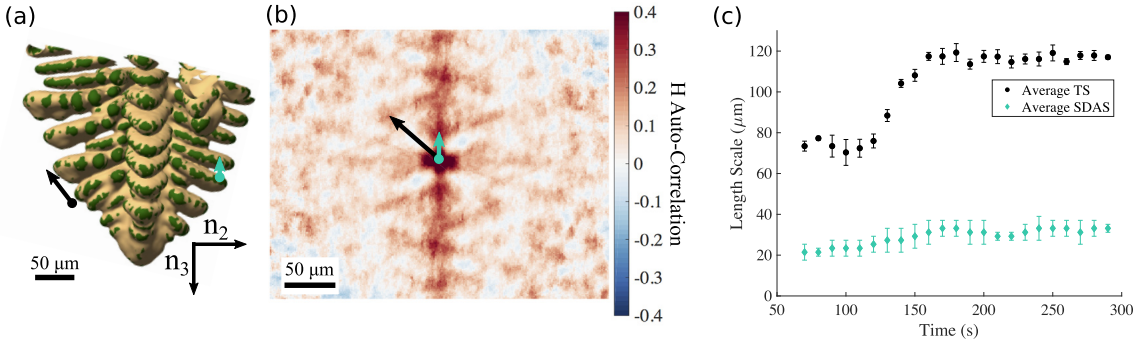

Fig. 4. (a) Al dendrite at 170 s. Dark green areas correspond to the top 20% mean curvatures values and the tan corresponds to every other mean curvature. The arrows illustrate the TS (black, ~ 117 μm) and the SDAS in the $\boldsymbol{n_3}$ direction (teal, ~ 31 μm); (b) *H* auto-correlation of the dark green and tan regions in the $\boldsymbol{n_2} - \boldsymbol{n_3}$ plane at 170 s. Black and teal arrows indicate the TS and SDAS, respectively; and (c) Temporal evolution of the average TS (black dots) and the average SDAS (teal diamonds). (For interpretation of the references to color in this figure, the reader is referred to the web version of this article.)

black arrow represents the average TS (117 ± 2 μm). The angle between the two arrows (~ 48°) is a quantitative measurement of the average dendrite tip profile.

Fig. 4c shows the evolution of the average TS (black) and SDAS evolution (teal). The TS is nearly constant (74 μm) up to 120 s, increases at a rate of ~ 1 μm/s up to 160 s, then reaches a nearly constant value (117 μm). At early times (up to 120 s), new side-branches are formed near the moving tip while existing branches continue to grow, with near-constant velocity, yielding a near-constant average TS [6]. Branches further away from the tip are longer (as shown in Fig. 1a and b), giving the dendrite a tree-like morphology. During this stage, the average TS is representative of the TS between all successive branches.

At intermediate times, external disturbances (such as convection in the liquid) cause some side-branches to stop growing while "active branches" accelerate their evolution [6]. As soon as a side-branch stalls, its growth is hindered due to the solute released by the surrounding branches. The active branches have more space to grow and eventually establish a larger TS. This side-branch competition is quantitatively measured in the H auto-correlation as a transition from the TS between successive branches (74 μm) to the TS between active branches (117 μm).

At late times (after 160 s), the dendrite tip strongly interacts with the diffusion field of the seaweed structure at the bottom of the sample, and the tip velocity is strongly reduced (0.4 μm/s). No new side-branches form near the tip while the existing active branches continue to grow away from the dendrite core. As side-branch competition is slowed considerably near the tip, the measured TS remains nearly constant for the remainder of the experiment.

The true SDAS is an average of the spacing between all successive branches (active and inactive). The SDAS measured using two-point statistics is nearly constant up to 120 s (~ 23 μm), slightly increases at a rate of ~ 0.1 μm/s until 160 s, then remains nearly constant (~ 32 μm). However, after 120 s, it is visually clear that no new side-branches form in the observed near-tip region, thus the true SDAS should not change. The measured SDAS is overestimated due to the effects of side-branch competition. As active arms grow and establish a larger active-to-active spacing, some of their curvatures contribute to the data used to measure SDAS. At the same time, as inactive branches erode away, their curvatures continuously decrease and thus contribute less to the two-point statistics. This decrease in curvature could also stem from errors in reconstruction, segmentation or smoothing. The net effect is an erroneous growth in the measured SDAS that qualitatively matches the trend observed in the TS. This is a limitation of using two-point statistics to measure SDAS.

The angle between the SDAS and TS was measured throughout growth as a nearly constant value of 49 ± 5°, where the error is the standard deviation in mean angle. This demonstrates that the average dendrite profile near the tip remains constant throughout the experiment. However, it is expected that the angle will increase at very late times due to the nearly-halted dendrite tip and faster-growing side-branches.

In conclusion, we showcase the use of two-point statistics as an efficient and un-biased tool for characterizing a solidifying Al-12.6 wt.% Cu alloy. The evolution of dendrite primary arm thickness, average SDAS, and average TS were tracked using two-point Pearson auto-correlations of scaled mean curvatures. This statistical technique identified side-branch competition phenomena in a growing dendrite, by showing a regime in which the average TS sharply increased and a new average TS was established. By comparing the SDAS and angle between average TS and SDAS, it is shown that the dendritic profile remains constant, independent of this competition process. This technique can be readily applied to a variety of growth experiments such as eutectic growth in Al-Ge [27] and dendritic growth in Mg-Sn [28]. Two-point statistics can also be used to analyze complex microstructural outputs generated by computational models such as phase field simulations of dendritic growth [29,30] and coarsening [31]. Thus, these quantitative measurements of microstructural evolution can enable the stringent verification of simulation codes needed for materials design.

Funding

This work was supported by the U.S. Department of Energy [DE-FG02-99ER45782]; and the Natural Sciences and Engineering Research Council of Canada (NSERC) [PGSD3-516809-2018]. Use of the Advanced Photon Source was supported by the U.S. Department of Energy, Office of Science, Office of Basic Energy Sciences [DE-AC02-06CH11357].

Declaration of Competing Interest

The authors declare that they have no known competing financial interests or personal relationships that could have appeared to influence the work reported in this paper.

Supplementary material

Supplementary material associated with this article can be found, in the online version, at doi:10.1016/j.scriptamat.2020.02.034.

References

[1] J.W. Gibbs, K.A. Mohan, E.B. Gulsoy, A.J. Shahani, X. Xiao, C.A. Bouman, M. De-Graef, P.W. Voorhees, Sci. Rep. 5 (2015) 11824.
[2] M.E. Glicksman, Metall. Mater. Trans. A 43 (2011) 391–404.
[3] M.S. Turhal, T. Savaskan, J. Mater. Sci. 38 (2003) 2639–2646.
[4] R. Ahmad, M.B.A. Asmael, N.R. Shahizan, S. Gandouz, Int. J. Min. Met. Mater. 24 (2017) 91–101.
[5] S.C. Huang, M.E. Glicksman, Acta Metall. 29 (1981) 701–715.
[6] S.C. Huang, M.E. Glicksman, Acta Metall. 29 (1981) 717–734.
[7] R. Mendoza, J. Alkemper, P.W. Voorhees, Metall. Mater. Trans. A 34 (2003) 481–489.
[8] R. Mendoza, I. Savin, K. Thornton, P.W. Voorhees, Nat. Mater. 3 (2004) 385–388.
[9] R. Mendoza, J. Alkemper, P.W. Voorhees, Z. Metallkd. 96 (2005) 155–160.
[10] D. Kammer, P.W. Voorhees, Acta Mater. 54 (2006) 1549–1558.
[11] R.N. Grugel, J. Mater. Sci. 28 (1993) 677–683.
[12] Y. Sun, A. Cecen, J.W. Gibbs, S.R. Kalidindi, P.W. Voorhees, Acta Mater. 132 (2017) 374–388.
[13] Y. Sun, W.B. Andrews, K. Thornton, P.W. Voorhees, Sci. Rep. 8 (2018) 17940.
[14] Y. Sun, Spatio-Temporal Analysis of Coarsening in Complex Microstructures Using Two-Point Statistics, Ph.D. thesis, Northwestern University, 2018.
[15] Y. Sun, K.L.M. Elder, P.W. Voorhees, IOP Conf. Ser. Mater. Sci. Eng. 580 (2019) 012011.
[16] R. Trivedi, J. Cryst. Growth 49 (1980) 219–232.
[17] K.A. Mohan, S.V. Venkatakrishnan, J.W. Gibbs, E.B. Gulsoy, X. Xiao, M. De Graef, P. Voorhees, C.A. Bouman, IEEE Trans. Comput. Imaging 1 (2015) 96–111.
[18] N. Otsu, IEEE Trans. Syst. Man Cybern. 9 (1979) 62–66.
[19] D.A. Porter, K.E. Easterling, M.Y. Sherif, Phase Transformations in Metals and Alloys, CRC Press, 2009.
[20] J. Zhang, S.O. Poulsen, J.W. Gibbs, P.W. Voorhees, H.F. Poulsen, Acta Mater. 129 (2017) 229–238.
[21] L.K. Aagesen, J.L. Fife, E.M. Lauridsen, P.W. Voorhees, Scr. Mater. 64 (2011) 394–397.
[22] J.H. Lee, S. Liu, H. Miyahara, R. Trivedi, Metall. Mater. Trans. 35 (2004) 909–917.
[23] U. Dahlborg, M. Besser, M. Calvo-Dahlborg, S. Janssen, F. Juranyi, M. Kramer, J. Morris, D. Sordelet, J. Non-Cryst. Solids 353 (2007) 3295–3299.
[24] B. Zhang, A. Griesche, M. A., Phys. Rev. Lett. 104 (2010) 035902.
[25] C.-L. Park, P.W. Voorhees, K. Thornton, Comput. Mater. Sci. 85 (2014) 46–58.
[26] J.W. Gibbs, P.W. Voorhees, IMMI 3 (2014) 73–84.
[27] A.J. Shahani, X. Xiao, P.W. Voorhees, Nat. Commun. 7 (2016) 12953.
[28] S. Shuai, E. Guo, A.B. Phillion, M.D. Callaghan, T. Jing, P.D. Lee, Acta Mater. 118 (2016) 260–269.
[29] T. Takaki, S. Sakane, M. Ohno, Y. Shibuta, T. Shimokawabe, T. Aoki, ISIJ Int. 56 (2016) 1427–1435.
[30] T. Pusztai, G. Bortel, L. Granasy, Mater. Sci. Eng. A 413-414 (2005) 412–417.
[31] T. Cool, P.W. Voorhees, Philos. Trans. R. Soc. A 376 (2018) 2113.